Acta Pharmaceutica Sinica B 2026;16(7):4426−4441

Chinese Pharmaceutical Association
Institute of Materia Medica, Chinese Academy of Medical Sciences

Acta Pharmaceutica Sinica B

www.elsevier.com/locate/apsb
www.sciencedirect.com

ORIGINAL ARTICLE

Targeting FAPα-positive hepatic stellate cells ameliorates the formation of pre-metastatic niche

Sishan Yan[a,b,c,†], Jingwen Xie[a,b,c,†], Lijuan Deng[d,†], Chulong Chen[a,b,c], Wenfeng Mai[e], Shuran Fan[a,b,c], Runyu Liu[a,b,c], Maohua Huang[a,b,c], Xiaobo Li[a,b,c], Junqiu Zhang[a,b,c], Shuai Han[f], Zhongshun Tang[f], Wenqian Yin[a,b,c], Qun Miao[a,b,c], Chunlin Fan[a,b,c], Wencai Ye[a,b,c], Changzheng Shi[e,*], Dongmei Zhang[a,b,c,*], Ming Qi[a,b,c,e,*], Minfeng Chen[a,b,c,*]

[a]*State Key Laboratory of Bioactive Molecules and Druggability Assessment, Guangdong Basic Research Center of Excellence for Natural Bioactive Molecules and Discovery of Innovative Drugs, Jinan University, College of Pharmacy, Guangzhou 510632, China*
[b]*Guangdong−Hong Kong−Macau Joint Laboratory for Pharmacodynamic Constituents of TCM and New Drugs Research, Jinan University, Guangzhou 510632, China*
[c]*Guangdong Province Key Laboratory of Pharmacodynamic Constituents of TCM and New Drugs Research, Jinan University, Guangzhou 510632, China*
[d]*School of Traditional Chinese Medicine, Jinan University, Guangzhou 510630, China*
[e]*The First Affiliated Hospital of Jinan University, Guangzhou 510632, China*
[f]*General Surgery Center, Zhujiang Hospital, Southern Medical University, Guangzhou 510282, China*

Received 21 July 2025; received in revised form 30 September 2025; accepted 26 October 2025

KEY WORDS

Pre-metastatic niche;
Metastasis;
FAPα;

Abstract The pre-metastatic niche (PMN) serves as a catalyst for tumor metastasis and colonization, involving communication between immune cells and stromal cells. However, less is known about the specific cell-type and their organ-specific functions in PMN formation, with available therapeutic strategies still limited. Here, we identified a significant expression of fibroblast activation protein alpha (FAPα) in hepatic stellate cells (HSCs) associated with the formation of liver PMN, which was dramatically

*Corresponding authors.
E-mail addresses: minfengchen@jnu.edu.cn (Minfeng Chen), qiming@jnu.edu.cn (Ming Qi), dmzhang701@jnu.edu.cn (Dongmei Zhang), sczcn@126.com (Changzheng Shi).
[†]These authors made equal contributions to this work.
Peer review under the responsibility of Chinese Pharmaceutical Association and Institute of Materia Medica, Chinese Academy of Medical Sciences.

https://doi.org/10.1016/j.apsb.2026.04.018

Hepatic stellate cell;
ECM remodeling;
Macrophage;
FAPα-activated prodrug;
NLRP3 inflammasome

attenuated in HSC-specific conditional *Fap*-knockout mice. Mechanistically, tumor cell-derived exosomal miR-2467-3p upregulated FAPα expression in HSCs. FAPα^+ HSCs promoted IL-18 secretion *via* NF-κB/NLRP3/caspase-1 signaling pathway, which facilitated extracellular matrix (ECM) remodeling and macrophage recruitment. By targeting FAPα^+ HSCs, the FAPα-activated prodrug Z-GP-DAVLBH disrupted the PMN and suppressed tumor liver metastasis. Collectively, our study emphasizes the crucial role of FAPα^+ HSCs in the liver PMN and provides a promising therapeutic strategy for tumor metastasis.

1. Introduction

Distal metastasis is a major cause of mortality for tumor patients[1], and the occurrence of organ tropism depends on the formation of pre-metastatic niche (PMN). Before tumor cells arrive, PMN, a tumor cell-friendly microenvironment was established, favoring the settlement and colonization of metastatic tumors as "soil"[2], typically characterized by increased vascular permeability, angiogenesis, immune cell infiltration, and extracellular matrix (ECM) remodeling[3−5]. Moreover, metastatic recurrence in patients is also associated with the distal educational role of PMN. Inhibiting PMN formation may represent an effective strategy for the treatment of tumor metastasis. Research has demonstrated that PMN formation is related to extracellular vehicles (EVs), chemokines, and metabolites from primary tumors, and the microenvironment change of secondary metastatic organs[6,7]. Nevertheless, druggable targets for PMN remain deficient; dissection of the key cellular components that promote PMN formation in secondary metastatic organs is expected to deepen the understanding of the mechanisms of PMN formation and develop promising therapeutic strategies.

Liver metastases occur in up to 50% of patients with metastatic tumors[8]. Complex interactions between tumor cells and the liver microenvironment accelerate the formation of liver PMN and tumor metastasis. A variety of cellular and molecular components are involved in the formation of liver PMN, including bone marrow-derived cells, hepatic stellate cells (HSCs), macrophages, ECM, and tumor-derived factors[9]. HSCs, considered as liver-specific pericytes[10], upon activation, regulate ECM remodeling and immune homeostasis by secreting growth factors, cytokines, and other components, thereby facilitating tumor liver metastasis[11]. However, there is still a lack of specific targets and effective therapeutic strategies targeting HSCs to inhibit PMN formation.

Fibroblast activation protein α (FAPα) is a type II integral membrane serine protease that has the capacity to cleave N-terminal benzyloxy carbonyl-blocked (Z-blocked) Gly-Pro (Z-GP) dipeptide linkages[12]. FAPα has been reported to promote fibrosis and liver inflammation in HSCs[13]. In the tumor environment, FAPα^+ HSCs contribute to immunosuppression, promoting tumor liver metastasis[14]. Yet the prevalence and significance of FAPα^+ HSCs in PMN remain undefined. Indubitably, FAPα is identified as one of the most promising targets in tumor therapy. Strategies for FAPα are targeted by inhibitors of the enzyme activity, including small molecule inhibitors[15], Gallium 68 (^{68}Ga)-labeled FAPI[16], and monoclonal antibodies[17]. Given the limited selectivity of these therapeutic strategies, exploring the novel therapeutic approach targeting FAPα^+ HSCs will provide clues to suppress tumor metastasis.

Here, we found that FAPα was highly expressed in HSCs of the liver PMN, which promoted PMN formation. Mechanistically, tumor cell-derived exosomal miR-2467-3p increased the expression of FAPα in HSCs. FAPα^+ HSCs activated NF-κB/NLRP3/caspase-1/IL-18 pathway through an enzyme-dependent manner, thereby promoting ECM remodeling and recruiting macrophages to facilitate the formation of the PMN. Targeting FAPα^+ HSCs with the FAPα-activated prodrug Z-GP-DAVLBH effectively inhibited liver PMN formation and reduced tumor metastasis. These findings provide new insights into the mechanisms of PMN formation and propose an alternative therapeutic strategy to combat tumor metastasis.

2. Materials and methods

2.1. Cell lines and cell culture

Human colorectal carcinoma cell line (HCT116) was obtained from ATCC (Rockville, MD, USA), and LM-HCT116 cells were constructed by our lab[18]. LX-2, a normal human hepatic stellate cell line, was purchased from Sure Biological Technology (Beijing, China). The mouse colorectal carcinoma cell line (MC38) and the mouse pancreatic cancer cell line (Panc02) were purchased from BeNa Culture Collection (Beijing, China) and iCell Bioscience Inc. (Shanghai, China), respectively. The aforementioned cells were cultured in DMEM (Gibco, Carlsbad, CA, USA) with 10% FBS (ExCell Bio, Shanghai, China) and 1% penicillin−streptomycin (Gibco) at 37 °C with 5% CO_2. Human monocytic leukemia cell line THP-1 (ATCC) was cultured in RPMI-1640 medium (Gibco) supplemented with 10% FBS and 1% penicillin−streptomycin (Gibco).

2.2. Animals

Male C57BL/6 mice and BALB/c-Nu mice, five to six weeks old, were bought from BesTest Bio-Tech (Zhuhai, China). C57BL/6-*Fap*$^{fl/fl}$ mice (T052266), and *Gfap*-Cre mice (T004857) were purchased from GemPharmatech (Nanjing, China). Peers of *Fap*$^{fl/fl}$ mice were used as wild-type controls. All experiments were approved by the Institute of Experimental Animal Ethics Committee of Jinan University (Approval number: IACUC-20230515-09), and animals were maintained under a specific pathogen-free facility.

2.3. In vivo experiments

For the establishment of the PMN model, HCT116-luc, MC38-luc, MC38, and Panc02 were resuspended in PBS at a concentration of

5×10^6cells/mL, and a total of 5×10^5 tumor cells in 100 μL were gently injected into the spleens of mice. *Fap*$^{\Delta Gfap}$ (G*fap-Fap* knockout) mice were generated by crossing *Gfap*-Cre mice and *Fap*$^{fl/fl}$ mice and induced by tamoxifen (100 mg/kg, i.g., Beyotime, Shanghai, China) once every other day for a total of 3 times. For the *Nlrp3*-knockout in HSCs *in vivo*, adeno-associated virus (AAV) recombinant genomes were packaged in serotype 8 capsids, 5×10^{10} vector genome (vg) AAV particles were resuspended in 200 μL PBS. *Gfap*-Cre mice were administered *via* intravenous (i.v.) injection with AAV-shCTL or AAV-sh*Nlrp3* (Genechem, Shanghai, China). For therapeutic administration, mice bearing HCT116-luc xenografts were treated with Z-GP-DAVLBH (2 mg/kg, i.v.) once every other day for 14 days.

2.4. DNA extraction and analysis

The genomic DNA from tail snips was extracted by StarSpin Universal DNA Kit (Genstar, Beijing, China) and was analyzed by PCR assay using 2 × Taq PCR StarMix (Genstar). The DNA fragments were separated on 2% agarose gels. All primer sequences for PCR analysis are listed in Supporting Information Table S1.

2.5. Cell transfection and stimulation

HCT116-luc and MC38-luc cells were transfected with lentivirus luciferase vector GV260 (Ubi-MCS-firefly Luciferase-IRES-Puromycin, Genechem). Plasmids and small interfering RNA (siRNA) were transfected using Lipofectamine 3000 (Thermo Fisher Scientific, Waltham, MA, USA) according to the manufacturer's protocol. LX-2^{Vector} or LX-2^{FAP} cells were transfected with vector or FAP plasmids, respectively. LX-2^{FAP} cells were treated with a FAPα inhibitor SP-13786 (50 μmol/L, T7890, TargetMol, Shanghai, China) for 30 min. Gene knockdown in LX-2^{Vector} and LX-2^{FAP} cells was achieved by infection with shRNA plasmids or transfection with siRNAs, using corresponding negative controls as references. The sequences of all plasmids and siRNA are listed in Supporting Information Tables S2 and S3. LX-2^{Vector} and LX-2^{FAP} cells were stimulated with an NLRP3 inhibitor MCC950 (1 μmol/L, T6887, TargetMol) for 1 h. THP-1 cells were differentiated to Mϕ by phorbol 12-myristate 13-acetate (PMA, 200 nmol/L, TQ0198, TargetMol) for 16 h.

2.6. Flow cytometry

Murine livers were obtained from mice after the injection of HCT116-GFP on Days 0, 7, and 14. Single cells were separated with collagenase I, II, IV, and hyaluronidase (Yeasen, Shanghai, China) and filtered with a 40 μm filter. After erythrocyte lysis, cells were blocked with anti-mouse CD16/32 antibody (BioLegend, San Diego, CA, USA) for 10 min and incubated with the antibody for 1 h on ice. Samples were analyzed by a BD FACSCanto flow cytometer[19]. The antibodies used are listed in Supporting Information Table S4.

2.7. Bioluminescence imaging of tumor growth

For bioluminescence imaging of tumor growth, mice were injected with D-luciferin (150 mg/kg, i.p., Yeasen) after anesthesia. Luminescence signals were measured by a PerkinElmer IVIS Lumina LT imaging system to display the tumor metastatic situation.

2.8. Cell migration and invasion assays

Cell migration and invasion assays were performed using the transwell system (Corning, New York, USA) containing polycarbonate filters with a pore size of 8 μm and 24-well Boyden chambers. The bottom chambers were seeded with LX-2 cells undergoing transfection or stimulation, and 100,000 Mϕs were seeded in the upper chambers. After the co-culture for 24 h, cells in the chambers were fixed with 4% paraformaldehyde for 30 min and stained with 0.1% crystal violet solution for 5 min. For the invasion assays, 30 μL diluted Matrigel (Matrigel:PBS = 1:5, Yeasen) was added to the upper chambers, and then the following processes were performed in the same way. All the images were captured using an Olympus BX53 inverted epifluorescence microscope.

2.9. Wound healing assay

PKH67 (MIDI67, Sigma, Darmstadt, Germany)-labeled LX-2^{Vector} or LX-2^{FAP} cells were seeded into both sides of 3-well ibidi culture (ibidi, Gräfelfing, Germany), and PKH26 (MINI26, Sigma)-labeled Mϕs were seeded into the middle of a 3-well ibidi culture. After cells adhered, 3-well ibidi cultures were removed, and the wound width area was observed by a ZEISS Axiocam 506 color microscope after 24 h.

2.10. Western blot analysis

The cells were harvested using RIPA lysis buffer containing protease and phosphatase inhibitors (TargetMol), and then lysed on ice for 30 min. Subsequently, the samples were centrifuged at 12,000 rpm (Centrifuge 5417R, Eppendorf, Hamburg, Germany) and 4 °C for 15 min. Total protein extraction was detected by a BCA assay (Thermo Fisher Scientific). An equal amount of protein was separated by SDS−PAGE and subsequently transferred to polyvinylidene fluoride (PVDF) membranes (Millipore, Billerica, MA, USA). Blocking with 5% BSA, the membranes were incubated with antibodies. The antibodies were listed in the Supporting Information Table S4.

2.11. RT-qPCR

Total RNA was isolated from cells (Omega Bio-Tek, Norcross, GA, USA), and then 2 μg of the extracted total RNA was used to synthesize cDNA using the StarScript III RT Mix with gDNA Remover Kit (Genstar) according to the manufacturer's instructions. As for cDNA synthesis of mRNA, cDNA was synthesized from 2 μg of total RNA and corresponding mRNA RT-primers by the mRNA First Strand cDNA Synthesis Kit (Genstar). For miRNA analysis, *miR-2467-3p* standard (sequences: AGCAGAGGCAGAGAGGCUCAGG) and other mRNA were reverse transcribed to cDNA by a miRNA First Strand cDNA Synthesis kit (Sangon Biotech, Shanghai, China). RT-qPCR was performed using a Roche System at 95 °C for 5 min, followed by 45 cycles of 95 °C for 10 s, 60 °C for 10 s, and 72 °C for 10 s. Relative mRNA levels were quantified using the comparative threshold cycle ($2^{-\Delta\Delta CT}$) method with ACTB as the reference gene. Each assay was performed independently three times. A *miR-2467-3p* standard curve was generated from C_t values of serially diluted *miR-2467-3p* standard cDNA and was used to quantify *miR-2467-3p* in EVs[20,21].

All sequences for cDNA synthesis and RT-qPCR were listed in the Supporting Information Tables S5 and S6.

2.12. Enzyme-linked immunosorbent assay (ELISA)

Human IL-18 ELISA Kit (NeoBioscience Technology, Shenzhen, China) and Human IL-1β ELISA Kit (Cloud-clone, Wuhan, China) were used to measure IL-18 and IL-1β levels in the cell culture supernatant. IL-18 levels in mouse peripheral blood were detected by QuantiCyto Mouse IL-18 ELISA kit (NeoBioscience Technology) according to the manufacturer's instructions.

2.13. H&E staining, masson staining, and immunofluorescence

Tissues were embedded in paraffin and cut into 4 μm sections. After deparaffinization and rehydration, nuclei were stained with hematoxylin dye solution, and cytoplasm was stained with eosin for H&E staining. For Masson staining, tissue sections were stained with Masson trichrome staining kit (Servicebio, Wuhan, China) according to the manufacturer's instructions. All images were obtained by an Olympus BX53 inverted epifluorescence microscope. For immunofluorescence, tissues were subjected to antigen retrieval using citric acid (pH 6.0) buffer after deparaffinization, rehydration, and permeabilized with 0.1% Triton X-100. Blocking with QuickBlock immunostaining blocking solution (Beyotime), sections were incubated with antibodies at 4 °C overnight and incubated with HRP-conjugated secondary antibodies for 1 h at room temperature the next day. TSAPLus Fluorescence Kit with iF488-Tyramide, iF555-Tyramide, or iF647-Tyramide (Servicebio) was used to incubate various antibodies[22]. Finally, sections were stained with DAPI for 15 min and imaged using a ZEISS LSM 800 confocal microscope. All antibodies were listed in the Supporting Information Table S4.

2.14. Immunocytochemistry

After being seeded in confocal dishes (Nest, Wuxi, China), cells were permeabilized with 0.1% Triton X-100 and blocked with QuickBlock immunostaining blocking solution (Beyotime). Then, cells were incubated with antibodies at 4 °C overnight and incubated with Alexa Fluor 488 Goat anti-Rabbit (Invitrogen, Carlsbad, CA, USA) or Alexa Fluor 594 Goat anti-Mouse (Invitrogen) for 1 h at room temperature on the next day. Subsequently, cells were stained with DAPI for 15 min and imaged by a ZEISS LSM 800 confocal microscope. All antibodies are shown in the Supporting Information Table S4.

2.15. Dual-luciferase reporter assay

Luciferase reporter vectors of h-TCF21-3UTR-wt and h-TCF21-3UTR-mu were introduced into 293T cells with either hsa-miR-2467-3p or a negative control (NC), respectively. After 48 h, luciferase activity was measured and normalized to the activity of Firefly luciferase (Fluc) and *Renilla* luciferase (Rluc) (Promega, Madison, WI, USA). All sequences for luciferase reporter vectors were listed in the Supporting Information Table S7.

2.16. Isolation, identification, and uptake of EVs

LM-HCT116 conditioned medium was used to isolate EVs and was centrifuged for 10,000 × *g* at 4 °C for 30 min to remove dead cells, and the supernatant was filtered by a 0.22 μm filter (Bioland, Hangzhou, China). Next, the portion was centrifuged at 120,000 × *g* and 4 °C for 30 min using the Optima XPN-100 Ultracentrifuge, and EVs were collected and washed in PBS before dissolution. Then, EVs were analyzed for the expression of HSP70, CD63, TSG101, CD9, and GM130 by Western blotting and by particle-tracking analysis using a Particle Metrix ZetaView. The morphology of EVs was determined by a Hitachi HT-7700 transmission electron microscope. To explore whether LX-2 cells uptake EVs derived from LM-HCT116 cells, LX-2 cells were cultured with PKH67-labeled EVs for 6 h and incubated with phalloidin (Thermo Fisher Scientific). Images were shot by a ZEISS LSM 800 confocal microscope.

2.17. PI assay

After treating Z-GP-DAVLBH (500 nmol/L) for 24 h, LX-2^{Vector} or LX-2^{FAP} cells were stained with PI and Hoechst (Beyotime) for 10 min and observed by a ZEISS Axiocam 506 color microscope.

2.18. Single-cell RNA sequencing, Gene Ontology analysis, and KEGG analysis

Single-cell RNA sequencing (scRNA-seq) analysis was done using R (v4.3.1; RRID: SCR_016341) and subsequently analyzed using the Seurat package (v4.3.0). Genes with low prevalence (<3) and cells with less prevalent genes (<200) were discarded. Low-quality cells were discarded when the count of expressed genes was below 200 or above 7500. Moreover, cells were removed when their erythrocyte gene expression exceeded 3%. The remaining 26,169 single cells were used in further analyses. After running principal component analysis, 20 components were used for both FindNeighbors and FindClusters, as well as uniform manifold approximation and projection (UMAP) dimension reduction. Resolution 0.8 was used with FindClusters, yielding 25 distinct clusters. We used known marker genes to define the 25 clusters into 10 cell types (HSCs, endothelial cells, cholangiocytes, hepatocytes, T cells, NK cells, B cells, macrophages, neutrophils, DC cells). The scRNA-seq database of paracancerous liver of colorectal cancer liver metastasis (CRCLM) was obtained from the ArrayExpress database (E-MTAB-12022), and the scRNA-seq database of donor liver was obtained from Gene Expression Omnibus (GEO, GSE159929, GSE189539). The RNA-sequencing data are available at GEO (GSE208091). Gene Ontology (GO) and KEGG analyses were performed using bioinformatics, an online platform for data analysis and visualization. The miRNA-seq database of highly or poorly metastatic tumor cell-derived EVs was obtained from GEO (GSE123710). miRNA prediction of TCF21 was performed using TargetScan and miRWALK. A Venn analysis was processed by the top 200 miRNA predictions in TargetScan, miRNAs whose accessibility was more than 0.5 in miWALK, and upregulated exosomal miRNAs in highly-metastatic tumor cells.

2.19. Statistical analysis

All experiments were performed at least 3 times, and statistical analysis was conducted using GraphPad Prism 8.0. Data are presented as mean ± standard error (SEM). The *P* value of two groups was calculated with a two-tailed unpaired *t*-test, and multiple groups were evaluated with one-way ANOVA. *P* value <0.05 was statistically significant.

3. Results

3.1. FAPα is highly expressed in HSCs in the liver PMN

Colorectal cancer (CRC) liver metastasis is a hematogenous metastasis, whereby tumor cells migrate to the liver *via* the spleen into the portal venous system[23,24]. Therefore, liver PMN was constructed by intrasplenic injection of HCT116 or MC38 cells. We observed metastatic foci in the transplant CRC model after a 14-day injection, but not in the 7-day model (Fig. 1A, Supporting Information Figs. S1 and S2A). Several relevant indicators were employed to characterize the construction of PMN[3]. Masson staining and immunofluorescence staining showed that PMN exhibited ECM remodeling, including the increased expression of collagen and fibronectin (Fig. 1B and C, Fig. S2B and S2C). Additionally, immunofluorescence staining showed the high infiltration of F4/80$^+$ macrophages and Gr-1$^+$ myeloid-derived suppressor cells (MDSCs), indicating an immunosuppressive microenvironment (Fig. 1D, Fig. S2D). Due to medical ethical constraints, PMN and healthy liver samples were not available. Therefore, we collected the single-cell RNA sequencing (scRNA-seq) data from donor liver (GSE159929 and GSE189539) and paracancerous liver of CRCLM (E-MATB-12022) as the control and PMN group[25−27](Fig. 1E). Using scRNA-seq analysis, 10 clusters of cells were identified, and the proportion of HSCs was significantly increased in the PMN group (Fig. 1F and G). Previous studies have reported that in cases of liver cirrhosis and fibrosis, HSCs express FAPα to promote disease progression. In addition, the expression of FAPα in HSCs was markedly increased in the PMN group (Fig. 1H). Furthermore, immunofluorescence staining showed that FAPα was extremely elevated in activated HSCs in PMN, while the phenomenon was absent in the control group (Fig. 1I, Fig. S2E).

As the liver is also a common distal metastatic organ for pancreatic cancer[28,29], a PMN model of pancreatic cancer was generated by the intrasplenic injection of Panc02 cells (Supporting Information Fig. S3A). Masson staining and immunofluorescence staining showed that collagen and fibronectin were upregulated (Fig. S3B and S3C). Additionally, analysis of immune cells showed that F4/80$^+$ macrophages and Gr-1$^+$ MDSCs were highly infiltrated in PMN of pancreatic cancer, but the infiltration of T cells was not changed (Fig. S3D). Furthermore, FAPα was highly expressed in activated HSCs in PMN of pancreatic cancer (Fig. S3E). Taken together, our results suggest that FAPα$^+$ HSCs may be associated with the formation of liver PMN.

3.2. FAPα$^+$ HSCs promote ECM remodeling and macrophage recruitment to facilitate the formation of liver PMN and tumor liver metastasis

To investigate the function of FAPα in the formation of PMN, a PMN model was constructed in *Fap* wild-type mice (*Fap*$^{fl/fl}$) and HSC-specific knockout *Fap* mice (*Fap*$^{\Delta Gfap}$) (Fig. 2A, Supporting Information Fig. S4). After a week's tamoxifen induction, MC38-luc or Panc02-luc cells were inoculated in *Fap*$^{fl/fl}$ and *Fap*$^{\Delta Gfap}$ mice, respectively. Masson and immunofluorescence staining revealed that *Fap*$^{\Delta Gfap}$ mice exhibited reduced deposition of collagen and fibronectin (Fig. 2B and C, Supporting Information Fig. S5A), revealing that HSC-specific *Fap*-knockout *in vivo* rehabilitated ECM remodeling in PMN. Immunofluorescence staining verified that *Fap*$^{\Delta Gfap}$ mice exhibited less infiltration of F4/80$^+$ macrophages or Gr-1$^+$ MDSCs compared with *Fap*$^{fl/fl}$ mice (Fig. 2D, Fig. S5B). Moreover, activated HSCs were reduced in *Fap*$^{\Delta Gfap}$ mice in the PMN (Fig. 2E). The above experiments indicated that FAPα$^+$ HSCs facilitated the formation of PMN. To further confirm the effect of FAPα on tumor metastasis, a long-term transplanted tumor model was constructed in transgenic mice. *Fap*-knockout in HSCs decreased tumor metastasis, characterized by a decrease in radiance and a reduction in the number and size of metastatic foci, compared to *Fap*$^{fl/fl}$ mice (Fig. 2F and G, Fig. S5C). Taken together, our findings suggest that FAPα$^+$ HSCs elevate ECM remodeling and develop an immunosuppressive microenvironment, facilitating the formation of liver PMN and liver tumor metastasis.

3.3. FAPα activates NF-κB/NLRP3/caspase-1 signaling pathway and induces IL-18 secretion in HSCs

To further explore the mechanism of the promotion in liver PMN by FAPα$^+$ HSCs, RNA-sequencing analysis of LX-2^{Vector} and LX-2^{FAP} cells was performed. KEGG pathway analysis indicated that the TOP 100 upregulated genes in LX-2^{FAP} cells were associated with the NF-κB signaling pathway and cytokine-cytokine receptor signaling pathway (Fig. 3A, Supporting Information Fig. S6A). GO analysis revealed an enrichment in cytokine-mediated signaling pathway (Fig. S6B). Subsequently, GO analysis of differentially expressed genes in HSCs from PMN and control subjects by scRNA sequencing revealed that PMN-HSCs were associated with an acute inflammatory response (Fig. 3B). The hepatic inflammatory response is associated with the activation of inflammatory vesicles[30]. Therefore, we assumed that FAPα$^+$ HSCs might activate NF-κB/NLRP3 signaling pathway. Western blotting assay confirmed that overexpression of FAPα in LX-2 cells significantly activated NF-κB/NLRP3 signaling, while only a slight, non-significant increase was observed in STAT3 expression (Fig. 3C, Fig. S6C and S6D). Immunocytochemistry showed an increasing co-expression of NLRP3 and FAPα in LX-2^{FAP} cells (Fig. 3D). Otherwise, the activation of NF-κB/NLRP3 signaling pathway was correlated with the enzyme activity of FAPα (Fig. 3C and D). NLRP3 inflammasome is a crucial regulator of environmental homeostasis and inflammatory balance *via* pro-inflammasome cytokines[31]. According to DEGs encoding cytokine in LX-2^{FAP} cells[14], the RT-qPCR assay indicated a high expression of IL-18 in LX-2^{FAP} cells (Fig. S6E). Western blotting and ELISA assays showed the increased expression and release of IL-18 in LX-2^{FAP} cells (Fig. 3C and E). By comparison, although IL-1β was also examined as another major cytokine downstream of NLRP3, its expression and secretion exhibited only minor changes that were not as pronounced as those observed for IL-18 (Fig. S6F−S6H). Consequently, FAPα activated the NF-κB/NLRP3/caspase-1/IL-18 signaling pathway in HSCs. Moreover, the *Fap*-deficient PMN model was performed to confirm whether FAPα activates the NLRP3/caspase-1/IL-18 signaling pathway. The concentration of IL-18 in the PMN peripheral blood was decreased in *Fap*$^{\Delta Gfap}$ mice in comparison to *Fap*$^{fl/fl}$ mice (Fig. 3F). The co-location of NLRP3, caspase-1, and IL-18 was reduced in activated HSCs in *Fap*$^{\Delta Gfap}$ mice, in comparison to *Fap*$^{fl/fl}$ mice (Fig. 3G and H). Taken together, these data reveal that FAPα activates the NF-κB/NLRP3/caspase-1 signaling pathway and facilitates IL-18 release in HSCs.

3.4. FAPα stimulates ECM remodeling and macrophage recruitment through the NLRP3/IL-18 pathway

Subsequently, we validated whether FAPα promoted PMN formation *via* NF-κB/NLRP3/caspase-1/IL-18 signaling pathway. GO analysis revealed an enrichment in cell-matrix adhesion

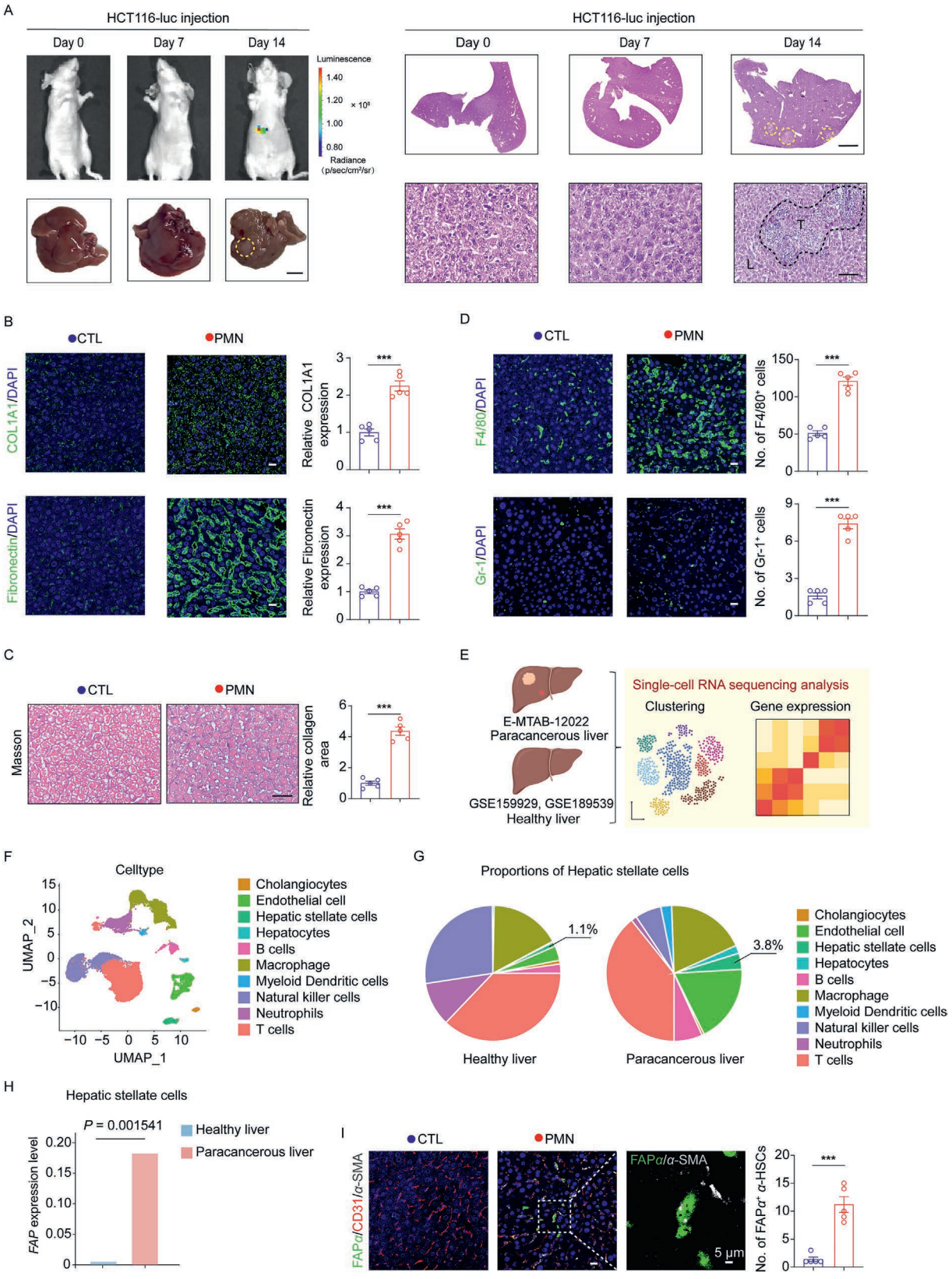

Figure 1 FAPα is highly expressed in the HSCs of the liver pre-metastatic niche. (A) The liver PMN was formed by the spleen injection of HCT116-luc cells in male BALB/c-nude mice. Scale bar, 5 mm. (B) Immunofluorescence staining and quantification of COL1A1 and Fibronectin in the liver PMN ($n=$ 5). Scale bar, 20 μm. (C) Masson staining of the control (CTL) and PMN liver ($n=$ 5). Scale bar, 50 μm. (D) Immunofluorescence staining and quantification of F4/80$^+$ or Gr-1$^+$ cells in the liver PMN ($n=$ 5). Scale bar, 20 μm. (E) Schematic diagram of scRNA sequencing analysis of paracancerous and healthy liver. (F) UMAP visualization of 26,169 single cells from liver tissues. (G) Pie chart of the

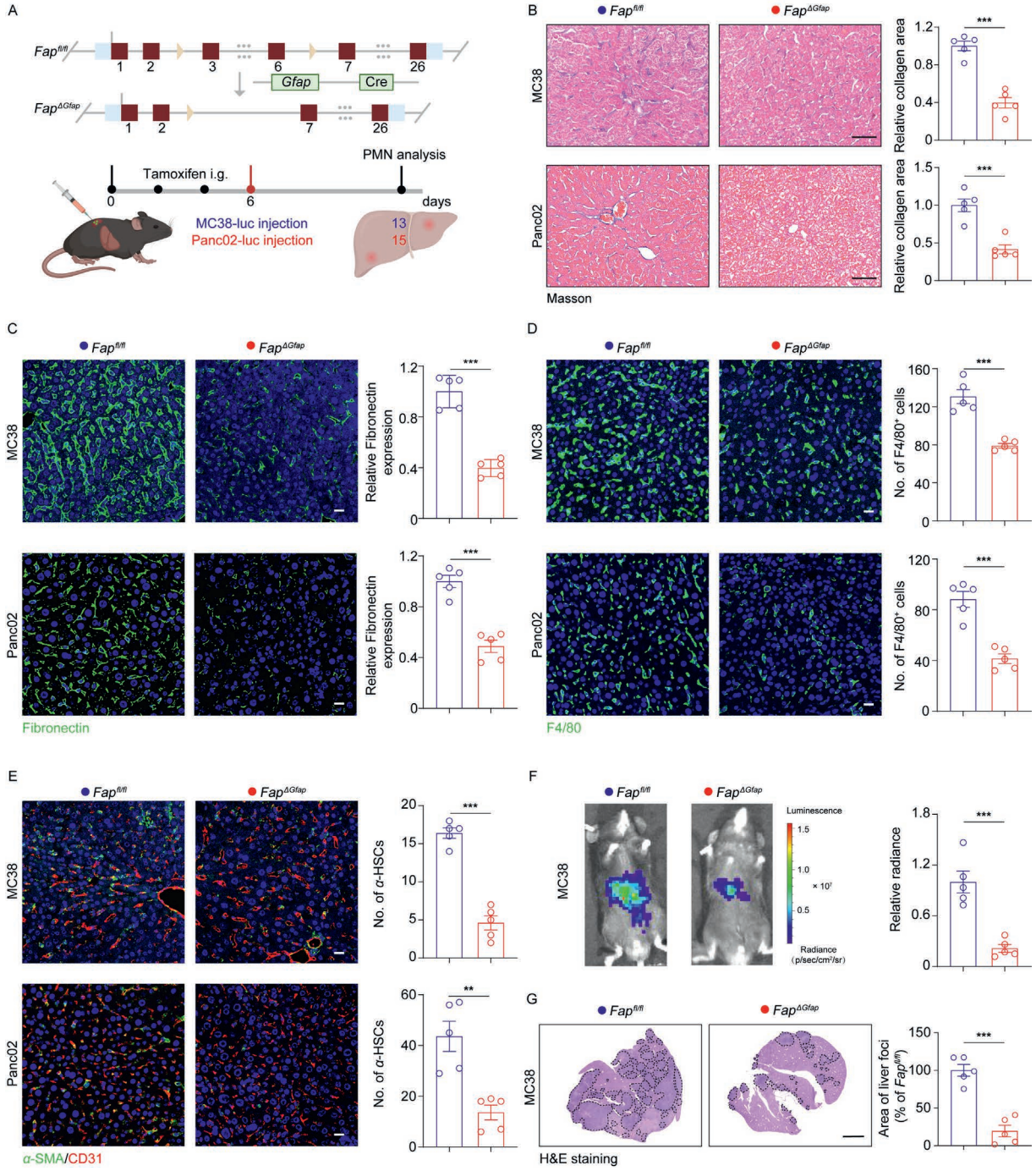

Figure 2 Conditional knockout of *Fap* in HSCs inhibits the formation of PMN and tumor metastasis. (A) The spleen injection of MC38-luc or Panc02-luc cells into $Fap^{fl/fl}$ or $Fap^{\Delta Gfap}$ mice. (B) Masson staining in the PMN of the CRC or pancreatic cancer in $Fap^{fl/fl}$ or $Fap^{\Delta Gfap}$ mice ($n = 5$). Scale bar, 50 μm. (C) Immunofluorescence staining and quantification of Fibronectin in the PMN of the CRC or pancreatic cancer in $Fap^{fl/fl}$ or $Fap^{\Delta Gfap}$ mice ($n = 5$). Scale bar, 20 μm. (D) Immunofluorescence staining and quantification of F4/80$^+$ macrophages in $Fap^{fl/fl}$ or $Fap^{\Delta Gfap}$ mice ($n = 5$). Scale bar, 20 μm. (E) Immunofluorescence staining and quantification of the αSMA$^+$HSCs (green) that adhered to the CD31$^+$ sinusoidal blood vessels (red) in $Fap^{fl/fl}$ or $Fap^{\Delta Gfap}$ mice. Scale bar, 20 μm. ($n = 5$). (F) Representative images of bioluminescence signals in $Fap^{fl/fl}$ or $Fap^{\Delta Gfap}$ mice with MC38-luc cells injection ($n = 5$). (G) Representative images and liver foci analysis of livers derived from MC38-luc-injecting $Fap^{fl/fl}$ or $Fap^{\Delta Gfap}$ mice ($n = 5$). Scale bar, 2 mm. Data are presented as mean ± SEM. $^{**}P < 0.01$, $^{***}P < 0.001$ b y two-tailed unpaired *t*-test.

cellular proportions of HSCs from healthy liver and paracancerous liver. (H) Expression of *FAP* in HSCs from healthy liver and paracancerous liver. (I) Immunofluorescence staining of FAPα (green) in αSMA$^+$HSCs (gray) attached to the CD31$^+$ sinusoidal blood vessels (red) in the liver PMN ($n = 5$). Scale bar, 20 μm. Data are presented as mean ± SEM. $^{***}P < 0.001$ b y two-tailed unpaired *t*-test.

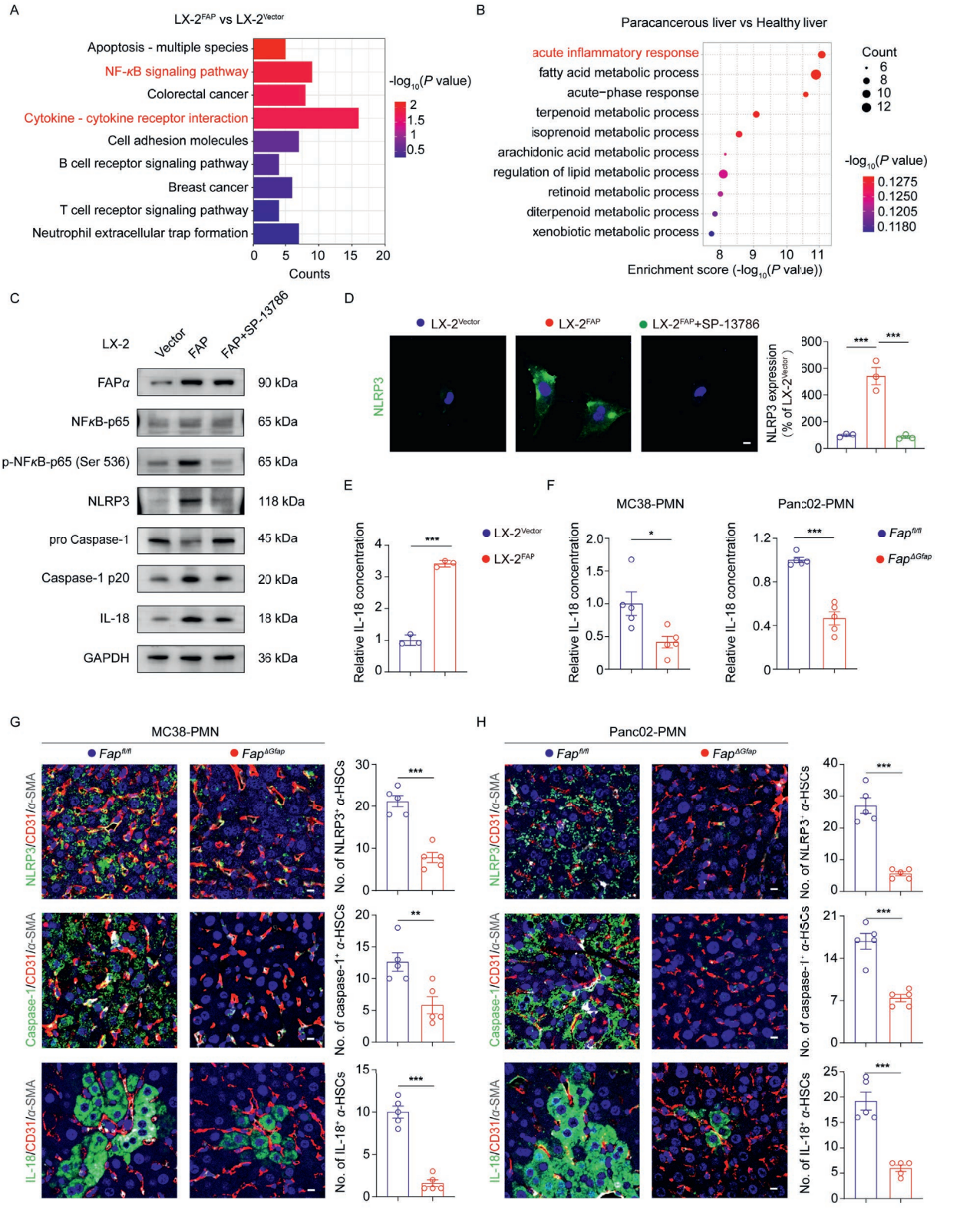

Figure 3 FAPα^+ HSCs upregulate NF-κB/NLRP3/caspase-1/IL-18 signaling pathway. (A) KEGG analysis of the Top100 upregulated genes in LX-2^{FAP} cells. (B) GO analysis of paracancerous and healthy HSCs from scRNA sequencing. (C) Western blotting analysis of FAPα, NFκB-p65, p- NFκB-p65, NLRP3, pro caspase-1, caspase-1 *P*20, IL-18 in LX-2^{FAP} cells with or without SP-13786 (n= 3). (D) Immunocytochemistry of NLRP3 in LX-2^{FAP} cells with or without SP-13786 (n= 3). Scale bar, 10 μm. (E) ELISA analysis of IL-18 concentration in LX-2^{FAP} cells (n= 3). (F) ELISA analysis of IL-18 in the peripheral blood of *Fap*$^{fl/fl}$ or *Fap*$^{\Delta Gfap}$ mice with MC38-luc or Panc02-luc injection (n= 5). (G, H) Immunofluorescence staining of NLRP3, caspase-1, or IL-18 (green) in αSMA$^+$HSCs (gray) that adhered to the CD31$^+$ sinusoidal blood vessels (red) in the PMN of CRC or pancreatic cancer (n= 5). Scale bar, 10 μm. Data are presented as mean ± SEM. *P< 0.05, **P< 0.01, ***P< 0.001 (one-way ANOVA with Tukey's *post hoc* comparison in D; two-tailed unpaired *t*-test in E−H).

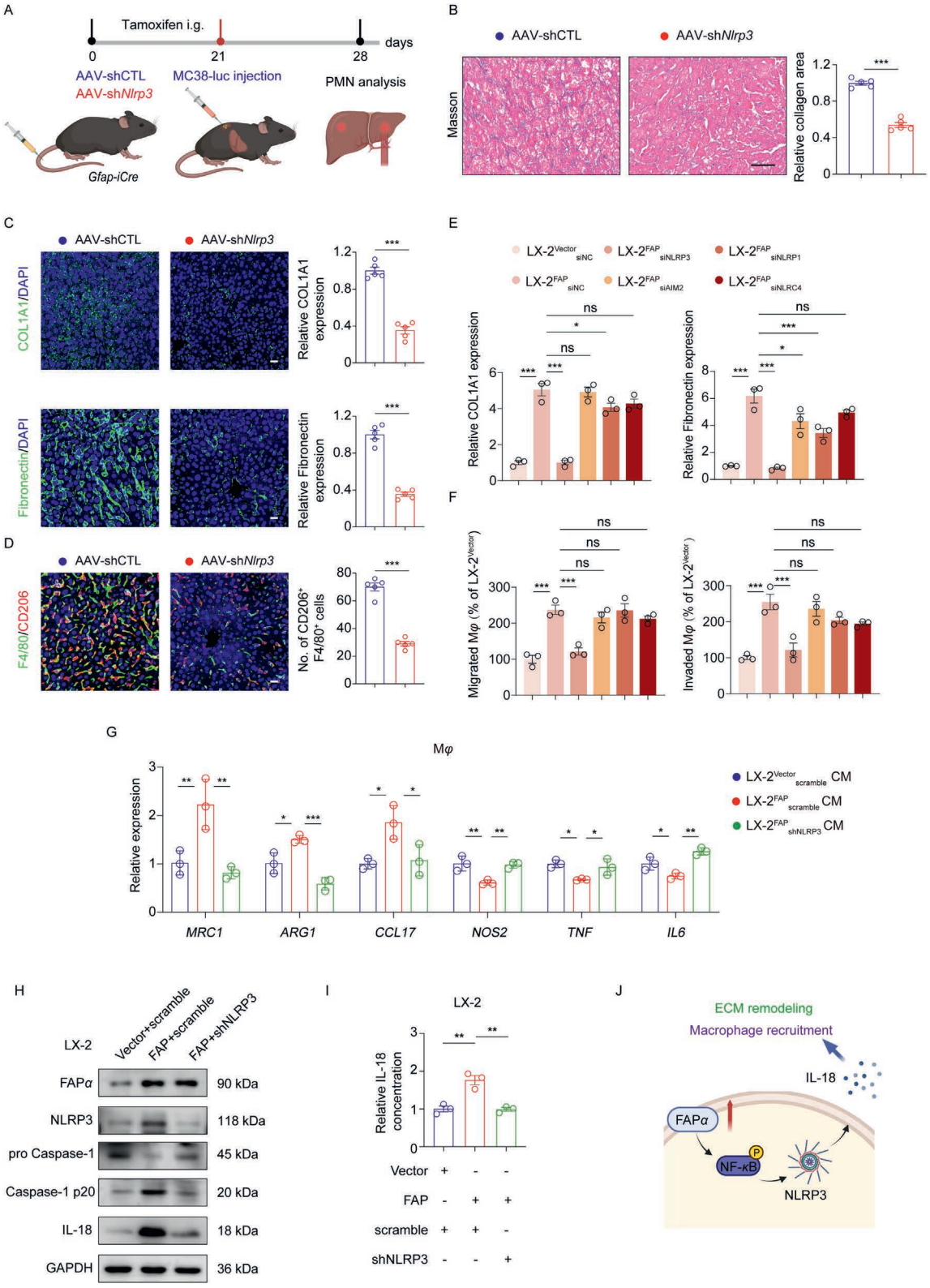

Figure 4 FAPα^+ HSCs induce ECM remodeling and macrophage infiltration *via* NLRP3. (A) The spleen injection of MC38-luc cells into AAV-shCTL or AAV-sh*Nlrp3* mice. (B) Masson staining in the PMN of the CRC or pancreatic cancer in AAV-shCTL or AAV-sh*Nlrp3* mice ($n=5$). Scale bar, 50 μm. (C) Immunofluorescence staining and quantification of COL1A1 and Fibronectin in the PMN of AAV-shCTL or AAV-sh*Nlrp3* mice ($n=5$). Scale bar, 20 μm. (D) Immunofluorescence staining and quantification of CD206$^+$ macrophages in the PMN of AAV-shCTL or AAV-sh*Nlrp3* mice ($n=5$). Scale bar, 20 μm. (E) Statistical analysis of immunocytochemistry of COL1A1 and Fibronectin in LX-2^{FAP} cells following knockdown of NLRP1, NLRP3, NLRC4, or AIM2 ($n=3$). (F) Transwell assays for the migration and invasion of Mϕ co-cultured with LX-2^{FAP} cells following knockdown of NLRP1, NLRP3, NLRC4, or AIM2 were added to the lower chambers of transwell plates

(Fig. S6B). A cell-cell communication analysis between HSCs and immune cells showed that HSCs had a predominant crosstalk with macrophages in the PMN (Supporting Information Fig. S7). Therefore, we further examined the ECM remodeling and macrophage recruitment. Immunocytochemistry showed an increasing expression of COL1A1 and fibronectin in LX-2^{FAP} cells (Supporting Information Fig. S8A). The transwell and wound healing assay showed that LX-2^{FAP} cells promoted the recruitment of macrophages (Fig. S8B and S8C). Furthermore, HSC-specific *Nlrp3*-knockout displayed that FAPα promoted ECM remodeling and macrophage recruitment *via* NLRP3 and IL-18 (Fig. 4A). Masson staining and immunofluorescence staining revealed that AAV-sh*Nlrp3* mice exhibited a reduction of collagen and fibronectin (Fig. 4B and C). Also, immunofluorescence staining showed a decrease in CD206$^+$ macrophages in AAV-sh*Nlrp3* mice (Fig. 4D). The above results revealed that HSC-specific *Nlrp3*-knockout *in vivo* reduced ECM remodeling and macrophage recruitment in PMN. To further confirm the dominant contribution of NLRP3 over other inflammasomes, we first analyzed the expression of several inflammasome components in LX-2 cells following FAPα overexpression. RT-qPCR results revealed a marked upregulation of NLRP3, while the expression of *NLRP1*, *NLRC4*, *AIM2*, and *IFI16* remained largely unchanged (Supporting Information Fig. S9A). Consistently, only NLRP3 knockdown markedly reduced IL-18 protein levels (Fig. S9B). Functionally, silencing NLRP3, but not other inflammasomes, significantly attenuated COL1A1 and fibronectin expression and impaired macrophage migration and invasion (Fig. 4E and F, Fig. S9C and S9D). These results further excluded the involvement of other inflammasome pathways and confirmed that NLRP3 plays a predominant role in FAPα-mediated ECM remodeling and immune cell recruitment. To further elucidate the role of NLRP3, we examined its effects on macrophage polarization and downstream signaling pathways. RT-qPCR assay exhibited a decreasing expression of M2 macrophage markers (*MRC1*, *ARG1*, *CCL17*) and an increasing expression of M1 macrophage markers (*NOS2*, *TNF*, *IL6*) when cultured with LX-2$^{FAP}{}_{shNLRP3}$ cells conditioned medium (Fig. 4G). Western blotting and RT-qPCR showed that knockdown of NLRP3 in LX-2^{FAP} cells inhibited the activation of the NLRP3/caspase-1/IL-18 pathway, and the secretion of IL-18 was also significantly affected after knockdown of NLRP3 (Fig. 4H and I, Fig. S9E and S9F). When treated with MCC950 (a NLRP3 inhibitor)[32], the recruitment of macrophages and the activation of the NLRP3/caspase-1/IL-18 pathway were rescued (Supporting Information Fig. S10). In addition, ECM remodeling and macrophage recruitment were attenuated when LX-2 cells were treated with IL-18 knockdown (Supporting Information Fig. S11A and S11B). Furthermore, RT-qPCR analysis revealed a downregulation of M2 macrophage markers (*MRC1*, *ARG1*, *CCL17*) and an upregulation of M1 markers (*NOS2*, *TNF*, *IL6*) in macrophages cultured with conditioned medium from LX-2$^{FAP}{}_{siIL\text{-}18}$cells (Fig. S11C). Taken together, FAPα facilitates ECM remodeling and macrophage recruitment *via* NLRP3 and IL-18 (Fig. 4J).

3.5. Tumor cell-derived exosomal miR-2467-3p upregulates the FAPα expression in HSCs

Accumulating evidence indicates that tumor cells secrete cytokines and EVs into distal metastatic organs to facilitate PMN formation[33−37]. To explore the mechanism of the upregulation of FAPα, we performed a co-culture experiment with tumor cells and HSCs. Western blotting and RT-qPCR assay showed that FAPα was increased in LX-2 cells cultured with the conditioned medium of liver metastatic-HCT116 (LM-HCT116) cells (Fig. 5A and B, Supporting Information Fig. S12A), whereas no significant change of FAPα expression was observed in LX-2 cells when cultured with an EVs-free medium (Fig. 5C, Fig. S12B). Therefore, we hypothesized that EVs may regulate FAPα expression in HSCs. EVs from LM-HCT116 cells were isolated and analyzed for the expression of CD63, TSG101, CD9, and GM130 by Western blotting (Fig. 5D). The transmission electron microscope image revealed a typical cup-shaped morphology of LM-HCT116 EVs, while the NTA assay showed that EVs had a diameter of 135.2 nm (Fig. 5E and F). EVs uptake assays showed that PKH67-labeled EVs were taken up into the cytosol of LX-2 cells (Fig. 5G). Subsequent stimulation with EVs for 12 h resulted in a pronounced elevation of protein and mRNA levels of FAPα in LX-2 cells. TCF21 has been identified as a deactivation factor of activated HSCs[38], so we speculated that TCF21 may be a crucial regulator of FAPα. Western blotting and RT-qPCR assay showed that TCF21 was decreased in EV-cultured LX-2 cells with an upregulation of FAPα (Fig. 5H and I, Fig. S12C). MicroRNAs (miRNAs) are an important component of EVs, which have a crucial role in tumor proliferation, metastasis, and drug resistance, and negatively regulate target genes[7]. We assumed exosomal miRNA would bind to TCF21 to regulate FAPα. A Venn analysis was conducted to miRNA prediction of TCF21 and upregulated exosomal miRNAs in highly-metastatic tumor cells, showing that miR-2467-3p may function as a regulator of TCF21 (Fig. 5J). The binding of miR-2467-3p and TCF21 was verified by a dual-luciferase reporter assay (Fig. 5K). RT-qPCR assay showed that *miR-2467-3p* was detected in EVs derived from LM-HCT116 cells and showed upregulation of *miR-2467-3p* in LX-2 cells cultured with EVs (Fig. 5L, Fig. S12D and S12E). The RNA level of *FAP* was decreased in EVs-cultured LX-2 cells with TCF21-overexpression (Fig. 5M, Fig. S12F). These results indicate that tumor cell-derived exosomal miR-2467-3p enhances FAPα expression in HSCs by downregulating TCF21.

3.6. Z-GP-DAVLBH targets FAPα^+ HSCs to disrupt the PMN formation and inhibit tumor liver metastasis

Despite many studies on the mechanisms of PMN, there is still a paucity of therapeutic strategies. Accordingly, we endeavored to target FAPα^+ HSCs, offering an innovative therapeutic strategy of PMN. After the intrasplenic injection of HCT116-luc cells, mice were administered with a FAPα-activated prodrug Z-GP-DAVLBH[39,40] (Fig. 6A). The results showed that administration of

($n=3$). (G) RT-qPCR analysis of MRC1, ARG1, CCL17, NOS2, TNF, IL6 in Mϕ cultured with CM from LX-2^{FAP} cells with or without NLRP3-knockdown ($n=3$). (H) Western blotting analysis of FAPα, NLRP3, pro caspase-1, caspase-1 *P*20, IL-18 in LX-2^{FAP} cells treated with or without NLRP3-knockdown ($n=3$). (I) ELISA analysis of IL-18 in LX-2^{FAP} cells processed through NLRP3-knockdown or not ($n=3$). (J) Mechanical diagram of FAPα^+ HSCs inducing ECM remodeling and macrophage infiltration. Data are presented as mean ± SEM. ns, no significance; *$P<0.05$, **$P<0.01$, ***$P<0.001$ (two-tailed unpaired *t*-test in B−D; one-way ANOVA with Tukey's *post hoc* comparison in E−G, I).

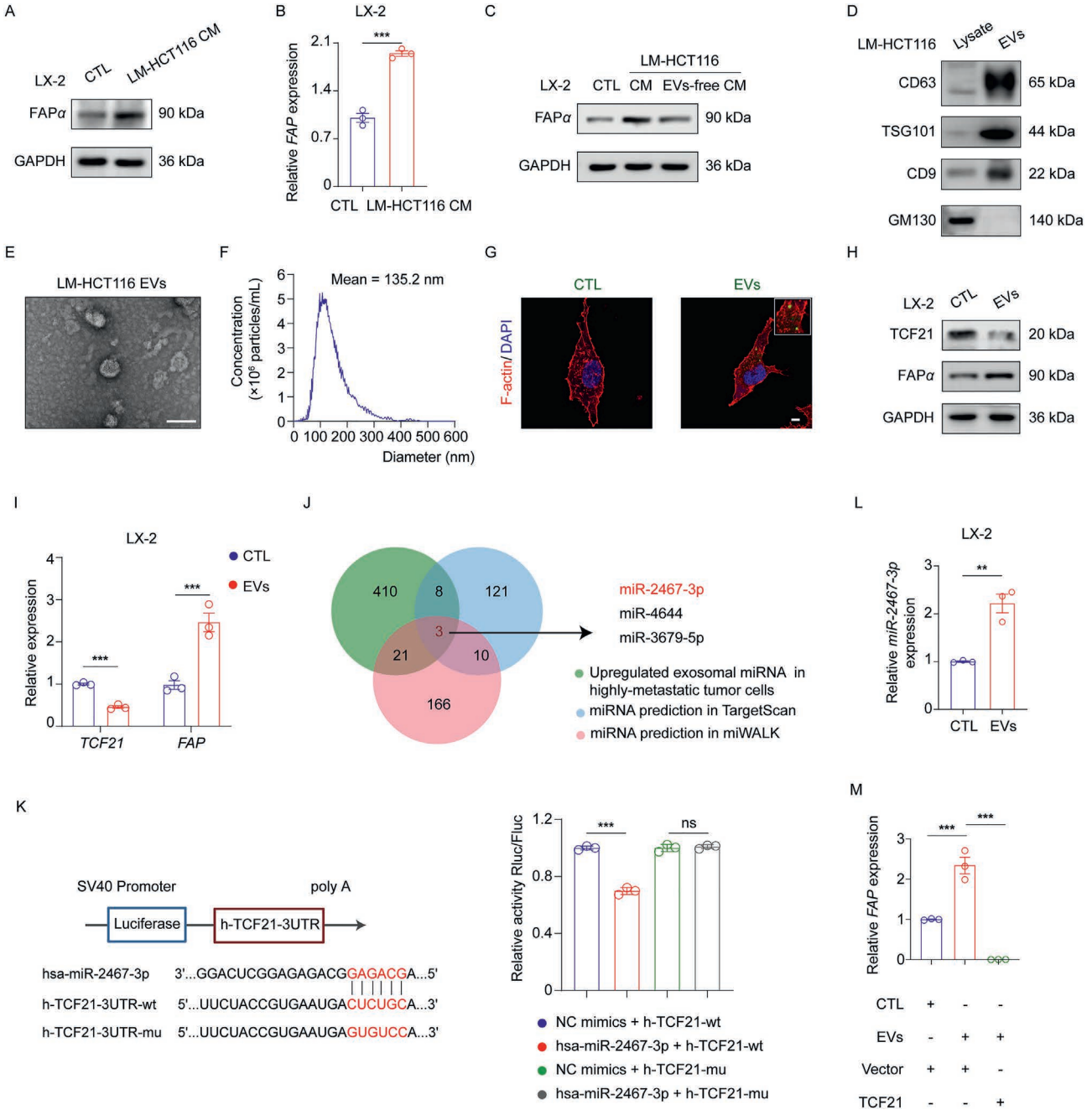

Figure 5 EVs derived from metastatic tumor cells drive the upregulation of FAPα in HSCs. (A) Western blotting analysis of the expression of FAPα in LX-2 cells treated with or without LM-HCT116 conditioned medium ($n=$ 3). (B) RT-qPCR analysis of the expression of *FAP* in LX-2 cells treated with or without LM-HCT116 conditioned medium ($n=$ 3). (C) Western blotting analysis of the FAPα expression in LX-2 cells treated with or without the EVs-free conditioned medium of LM-HCT116 ($n=$ 3). (D) The characterization and quantification by Western blotting analysis of the expression of CD63, TSG101, CD9, GM130 in the EVs derived from LM-HCT116. (E) The characterization and quantification by transmission electron microscope. Scale bar, 100 nm. (F) The measurement of EVs from LM-HCT116 by nanoparticle tracking analysis. (G) Uptake of PKH67 labeled-EVs in the LX-2 cells. Scale bar, 6 μm. (H) Western blotting analysis of the expression of TCF21, FAPα in LX-2 cells treated with or without LM-HCT116-EVs ($n=$ 3). (I) RT-qPCR analysis of the expression of *FAP* and *TCF21* in LX-2 cells treated with or without LM-HCT116 EVs ($n=$ 3). (J) A Venn analysis was conducted to miRNA prediction of TCF21 and highly-metastatic tumor cells-derived exosomal miRNAs. (K) A dual-luciferase reporter assay of TCF21 and miR-2467-3p. (L) RT-qPCR analysis of the expression of *miR-2467-3p* in LX-2 cells treated with or without LM-HCT116 EVs ($n=$ 3). (M) RT-qPCR analysis of the expression of *FAP* in EVs-cultured LX-2 cells with or without TCF21-overexpression ($n=$ 3). Data are presented as mean ± SEM. ns, no significance; $^{**}P<$ 0.01, $^{***}P<$ 0.001 (two-tailed unpaired *t*-test in B, I, L, K; one-way ANOVA with Tukey's *post hoc* comparison in M).

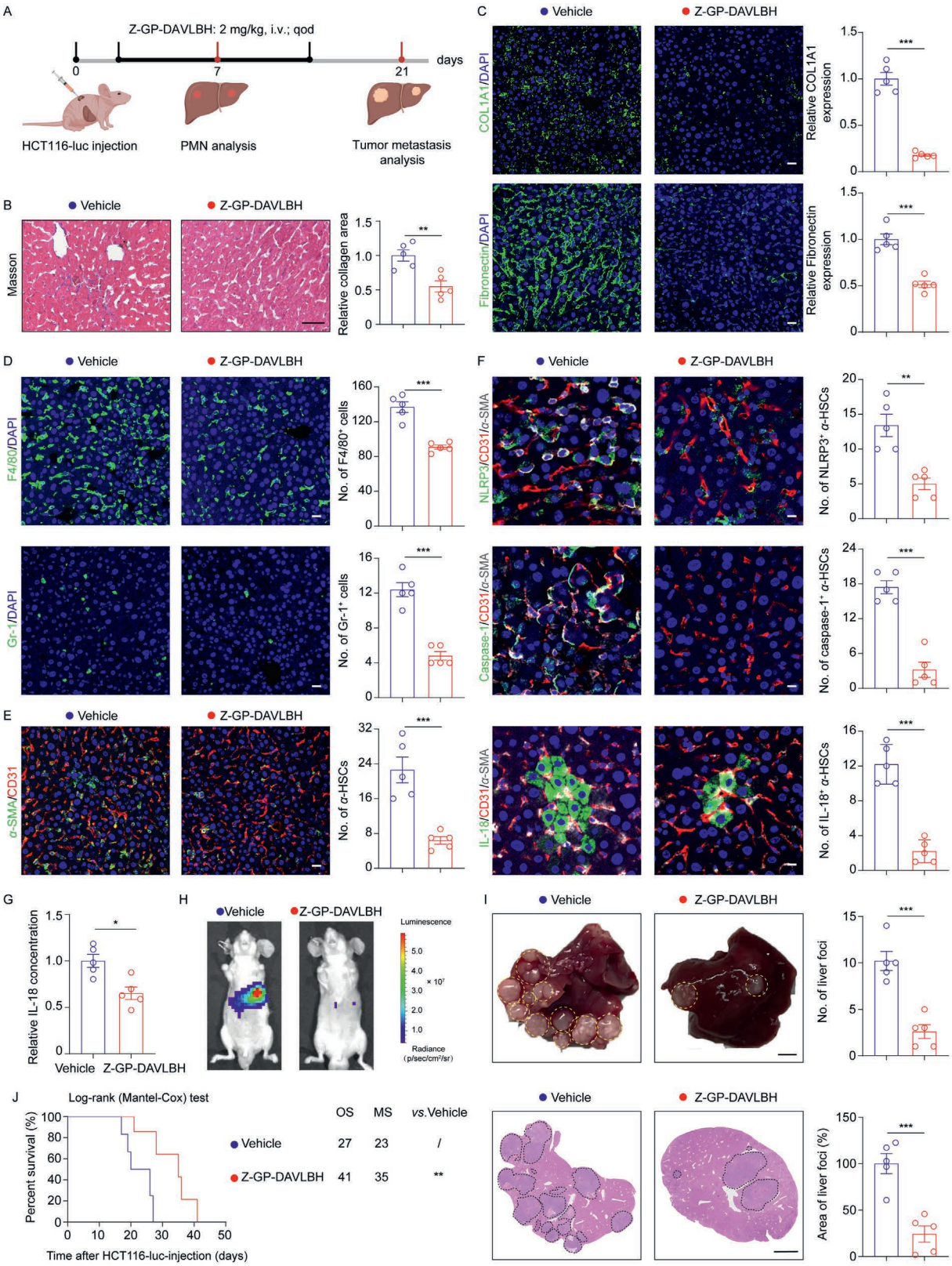

Figure 6 Targeting FAPα^+ HSCs to inhibit the formation of liver PMN and reduce CRCLM. (A) Therapeutic schedules for Z-GP-DAVLBH (2 mg/kg) treatment in mice bearing HCT116 cells. Livers in the period of PMN were attained for pathological analysis and tumors were harvested and photographed. (B) Masson staining in the PMN of the CRC (n = 5). Scale bar, 50 μm. (C) Immunofluorescence staining and quantification of COL1A1 and Fibronectin in the PMN of the CRC (n = 5). Scale bar, 20 μm. (D) Immunofluorescence staining and quantification of F4/80$^+$ or Gr-1$^+$ cells in the pre-metastatic niche of the CRC after Z-GP-DAVLBH treatments (n = 5). Scale bar, 20 μm. (E)

Z-GP-DAVLBH decreased collagen and fibronectin deposition and restored the immune microenvironment, characterized by the reduction of F4/80$^+$ macrophages and Gr-1$^+$ MDSCs (Fig. 6B−D). These results imply that Z-GP-DAVLBH treatment disrupts the PMN process by decreasing ECM remodeling and the number of immunosuppressive cells. Mechanistically, it was plausible that Z-GP-DAVLBH treatment induced apoptosis in LX-2^{FAP} cells (Supporting Information (Fig. S13A).Immunofluorescence staining displayed a reduction in the number of activated HSCs and a downregulation of the NLRP3/caspase-1/IL-18 pathway after Z-GP-DAVLBH-treatment (Fig. 6E and F). Moreover, the IL-18 level in peripheral blood had declined, a key indicator for evaluating the degree of PMN (Fig. 6G). In addition, Z-GP-DAVLBH exhibited no significant systemic toxicity, as evidenced by stable body weights and the absence of histopathological abnormalities in H&E-staining sections of the kidney, lung, heart, and spleen (Fig. S13B and S13C).

To confirm the effects of Z-GP-DAVLBH for inhibiting tumor metastasis, we performed a long-term Z-GP-DAVLBH treatment for CRC. The results revealed a decrease in radiance and a reduction in the number and size of metastatic foci in Z-GP-DAVLBH-treated mice (Fig. 6H and I). Furthermore, the survival curve analysis exhibited that Z-GP-DAVLBH treatment significantly prolonged the survival of mice bearing HCT116 xenografts (Fig. 6J). Consequently, our findings indicate that Z-GP-DAVLBH targeting FAPα^+ HSCs inhibits the NLRP3/caspase-1/IL-18 signaling pathway and ameliorates ECM remodeling and immunosuppressive microenvironment, thereby disrupting PMN and inhibiting the development of tumor liver metastasis.

4. Discussion

PMN represents an abnormal organ microenvironment that plays a crucial role in tumor migration and colonization before metastasis occurs[3,41]. Analyzing the regulatory mechanisms governing of cellular components within PMN during its formation can contribute to the development of novel therapeutic strategies to prevent tumor metastasis. The formation of the PMN is accompanied by widespread changes in the immune cell composition[42]. These changes likely contribute to the immunosuppressive environment that facilitates metastatic colonization. Although our study primarily focused on macrophages due to their significantly enhanced crosstalk with HSCs, as demonstrated by our comparative cell-cell communication analysis, we do not exclude the involvement of other immune cells. Neutrophils have been reported to facilitate PMN establishment by secreting pro-inflammatory cytokines and promoting ECM remodeling, which supports tumor cell colonization[43]. Similarly, NK cells play an essential role in metastatic control through their cytotoxic activity and immunosurveillance, which may be impaired in the immunosuppressive microenvironment[44]. These broader immune alterations merit further investigation, particularly regarding how they may be shaped or regulated by HSC-derived signals or other stromal components within the PMN.

HSCs play a critical role in liver diseases, including driving the liver PMN progression[45−47]. Nevertheless, the role of heterogeneous HSCs in the metastatic cascade is unclear. Single-cell sequencing reveals that activated HSCs could be classified as proliferative HSCs, inflammatory HSCs, intermediate activated or vascular HSCs, and contractile, migratory HSCs and fibrogenic myofibroblasts[48]. In our study, we found that KEGG analysis showed that CRCLM-paracancerous HSCs were related to inflammation, suggesting that the heterogeneity of HSCs might contribute to the PMN formation. And FAPα^+ HSCs activated NLRP3 and released the pro-inflammatory factor IL-18, having a crosstalk with macrophages, which indicated that activated HSCs may be involved in the progression of PMN as iHSCs. FAPα has been observed to exert different pro-tumor effects in different tumor microenvironments, which play important functions in regulating the immune microenvironment and ECM remodeling in tumor development[49]. For instance, FAPα^+ fibroblasts upregulate factors related to proliferation, inflammation, and ECM remodeling, and co-culture with endothelial cells enhances angiogenesis[50,51]. Other recent studies have demonstrated that FAPα^+ HSCs released CXCL5 to promote MDSC recruitment resistant to the angiogenesis inhibitor bevacizumab in CRC[14]. In our study, we found that FAPα^+ HSCs activated NLRP3 and released IL-18 in the PMN, contributing to the establishment of the ECM remodeling and macrophage recruitment, which are essential for the progression of PMN and tumor metastasis. Previous studies have demonstrated that hypoxia is associated with the upregulation of FAPα in the tumor microenvironment. However, adequate oxygenation in the PMN suggests that the upregulation of FAPα in HSCs may be caused by factors other than hypoxia. It has been demonstrated that HSCs took up EVs to accelerate CRCLM[45]. According to the crucial role of EVs in tumor metastasis, we hypothesized that the upregulation of FAPα in HSCs might be induced by EVs. Our data showed that tumor-derived exosomal miR-2467-3p was taken up, upregulating FAPα expression in HSCs by downregulating TCF21. Our findings thus corroborate the hypothesis that EVs play an important role in promoting PMN.

The anti-tumor effects of NLRP3 have been focused on immune cells, with limited investigation of stromal cells. A recent study showed that hyperactivation of NLRP3 in HSCs results in transdifferentiation into fibroblast phenotype, upregulating profibrotic genes and proteins and promoting liver fibrosis[52,53]. However, the activation and function of NLRP3 in HSCs within the tumor microenvironment remain unclear. In this study, we first demonstrated that FAPα activated NLRP3 in HSCs through an enzyme-dependent manner, thereby regulating ECM remodeling and the immune microenvironment in the PMN. Taken together, we found that HSCs released IL-18 after the NLRP3 activation in the PMN, promoting ECM remodeling and macrophage recruitment to facilitate tumor liver metastasis, bridging the gap in NLRP3 signaling in HSCs during tumor development. As demonstrated

Immunofluorescence staining of the αSMA$^+$HSCs (green) that adhered the CD31$^+$ sinusoidal blood vessels (red) in the pre-metastatic niche of the CRC after Z-GP-DAVLBH treatments. Scale bar, 20 μm. Quantification of the activated HSCs is shown (n= 5). (F) Immunofluorescence staining of NLRP3, caspase-1 or IL-18 (green) in αSMA$^+$HSCs (gray) that adhered the CD31$^+$ sinusoidal blood vessels (red) in the PMN of the CRC (n= 5). Scale bar, 10 μm. (G) ELISA analysis of IL-18 in the PMN of the CRC after Z-GP-DAVLBH treatments (n= 5). (H) Representative images of bioluminescence signals in the CRC livers after Z-GP-DAVLBH treatments (n= 5). (I) Representative images and analysis of liver foci from HCT116-luc-injecting mice (n= 5). Scale bar, 5 mm (top) and 2 mm (bottom). (J) The overall survival curves of mice bearing HCT116-injection treated with vehicle and Z-GP-DAVLBH (n= 5). Data are presented as mean ± SEM. *P< 0.05, **P< 0.01, ***P< 0.001 b y two-tailed unpaired t-test.

in previous research, NLRP3 is activated by EVs[54]. In this study, it was found that EVs increased FAPα expression, leading to NF-κB phosphorylation and NLRP3 activation. However, the specific downstream mediators of FAP enzymatic activity that link it to NLRP3 activation remain to be defined in future studies. The identification of this pathway offers a novel insight into NLRP3 function in HSCs within the tumor microenvironment.

Growing evidence demonstrates that targeting cellular components is a promising therapeutic strategy. COX-2$^+$ lung fibroblasts reprogram myeloid cells to exhibit dysfunction or immunosuppression, and the anti-metastatic activity of DC-based therapy effectively enhanced PD-1 blockade. Also, inhibition of macrophage infiltration may be beneficial for reducing the metastasis of primary tumors[19,55]. Nevertheless, therapeutic strategies for targeting activated HSCs remain limited. One of the therapeutic strategies against activated HSCs is targeting tumor-derived EVs with a TGF-β1 inhibitor, which still lacks specificity. Therefore, it is a significant challenge to target activated HSCs in the PMN. Here, we discovered a novel therapeutic strategy targeting activated HSCs using FAPα-prodrug Z-GP-DAVLBH to modulate the immunosuppressive environment and disrupt PMN. However, it is challenging to inhibit liver metastasis completely, and we are striving to deliver the combination therapy of Z-GP-DAVLBH and FDA-approved drugs to address it.

Despite growing research on the PMN, most studies are still limited to mouse models. In relation to our study and medical ethics, obtaining human normal and PMN liver tissue remains a significant challenge. Thus, in our study, we analyzed only scRNA-seq data from transplanted livers and paracancerous liver tissues from CRCLM, which may still differ from true PMN. Studying PMN *in vitro* is also difficult due to the complexity of the microenvironment. Therefore, an organ-chip model or microphysiological system may prove more suitable for studying PMN in the future.

5. Conclusions

In conclusion, our study revealed that FAPα in HSCs plays a pivotal role in establishing the liver PMN, which fosters tumor liver metastasis. These insights advance our understanding of PMN mechanisms and present a novel therapeutic approach for combating tumor metastasis.

Acknowledgments

This work was supported by the National Natural Science Foundation of China (grant numbers: U24A20815, 82404673, 82404652, 82473950, 82273941, 82204427, 82430108, and 82304526), National High-level Personnel of Special Support Program (Dongmei Zhang, Minfeng Chen, China), the Guangdong Basic and Applied Basic Research Foundation (grant numbers: 2024B1515020098, 2023B1515120023, 2025A1515011852 and 2024A1515013086, China), Science and Technology Projects in Guangzhou (grant numbers: 202102070001, SL2024A04J00374, and 2025A04J5158, China), China National Postdoctoral Program for Innovative Talents (grant number: BX20230144), Postdoctoral Fellowship Program of CPSF (grant number: GZB20230268, China), China Postdoctoral Science Foundation (grant number: 2023M741390 and 2025T180975), The Fundamental Research Funds for The Central Universities (grant number: 21624103, China) and K. C. Wong Education Foundation. We thank Xinqiang Lai from Analytical and Testing Center of Jinan University for instructions on flow cytometry analysis.

Author contributions

Minfeng Chen, Dongmei Zhang, Ming Qi, and Changzheng Shi designed and supervised the experiments. Minfeng Chen, Ming Qi, Sishan Yan, and Jingwen Xie drafted the manuscript. Lijuan Deng, Wencai Ye, Maohua Huang, Junqiu Zhang and Xiaobo Li revised the manuscript. Jingwen Xie, Sishan Yan, Lijuan Deng, Chulong Chen, Runyu Liu, Zhongshun Tang, Wenqian Yin and Qun Miao performed animal experiments, H&E staining, immunofluorescence analysis, and image acquisition and quantification. Wenfeng Mai performed bioinformatics analysis. Jingwen Xie, Runyu Liu, and Chulong Chen performed cell line experiments. Shuran Fan and Shuai Han performed bioluminescence image acquisition and analysis. Chunlin Fan performed Synthesis of Z-GP-DAVLBH.

Conflicts of interest

The authors declare no competing interests. Figures were created with BioRender.com.

Appendix A. Supporting information

Supporting information to this article can be found online at https://doi.org/10.1016/j.apsb.2026.04.018.

References

1. Dunbar KJ, Efe G, Cunningham K, Esquea E, Navaridas R, Rustgi AK. Regulation of metastatic organotropism. *Trends Cancer* 2025;**11**:216−31.
2. Nguyen DX, Bos PD, Massagué J. Metastasis: from dissemination to organ-specific colonization. *Nat Rev Cancer* 2009;**9**:274−84.
3. Liu Y, Cao X. Characteristics and significance of the pre-metastatic niche. *Cancer Cell* 2016;**30**:668−81.
4. Murgai M, Ju W, Eason M, Kline J, Beury DW, Kaczanowska S, et al. KLF4-dependent perivascular cell plasticity mediates pre-metastatic niche formation and metastasis. *Nat Med* 2017;**23**:1176−90.
5. Hongu T, Pein M, Insua-Rodríguez J, Gutjahr E, Mattavelli G, Meier J, et al. Perivascular tenascin C triggers sequential activation of macrophages and endothelial cells to generate a pro-metastatic vascular niche in the lungs. *Nat Cancer* 2022;**3**:486−504.
6. Zhang X, Zhang H, Gu J, Zhang J, Shi H, Qian H, et al. Engineered extracellular vesicles for cancer therapy. *Adv Mater* 2021;**33**: e2005709.
7. Kalluri R, LeBleu VS. The biology, function, and biomedical applications of exosomes. *Science* 2020;**367**. eaau6977.
8. Zhu C, Liao JY, Liu YY, Chen ZY, Chang RZ, Chen XP, et al. Immune dynamics shaping pre-metastatic and metastatic niches in liver metastases: from molecular mechanisms to therapeutic strategies. *Mol Cancer* 2024;**23**:254.
9. Wang Y, Jia J, Wang F, Fang Y, Yang Y, Zhou Q, et al. Pre-metastatic niche: formation, characteristics and therapeutic implication. *Signal Transduct Targeted Ther* 2024;**9**:236.
10. Pinzani M. Hepatic stellate (ITO) cells: expanding roles for a liver-specific pericyte. *J Hepatol* 1995;**22**:700−6.
11. Tang M, Zhang S, Yang M, Feng R, Lin J, Chen X, et al. Infiltrative vessel co-optive growth pattern induced by IQGAP3 overexpression promotes microvascular invasion in hepatocellular carcinoma. *Clin Cancer Res* 2024;**30**:2206−24.

12. Rosenblum JS, Kozarich JW. Prolyl peptidases: a serine protease subfamily with high potential for drug discovery. *Curr Opin Chem Biol* 2003;**7**:496−504.
13. Wang XM, Yu DMT, McCaughan GW, Gorrell MD. Fibroblast activation protein increases apoptosis, cell adhesion, and migration by the LX-2 human stellate cell line. *Hepatology* 2005;**42**:935−45.
14. Qi M, Fan S, Huang M, Pan J, Li Y, Miao Q, et al. Targeting FAPα-expressing hepatic stellate cells overcomes resistance to anti-angiogenics in colorectal cancer liver metastasis models. *J Clin Investig* 2022;**132**:e157399.
15. Pashaei M, Farhadi E, Kavosi H, Madreseh E, Enayati S, Mahmoudi M, et al. Talabostat, fibroblast activation protein inhibitor, attenuates inflammation and fibrosis in systemic sclerosis. *Inflammopharmacology* 2024;**32**:3181−93.
16. Chen J, Zhou Y, Pang Y, Fu K, Luo Q, Sun L, et al. FAP-targeted radioligand therapy with ^{68}Ga/^{177}Lu-DOTA-2P(FAPI)$_2$ enhance immunogenicity and synergize with PD-L1 inhibitors for improved antitumor efficacy. *J Immunother Cancer* 2025;**13**:e010212.
17. Yoshida S, Hayashi H, Kawahara T, Katsuki S, Kimura M, Hino R, et al. A vaccine against fibroblast activation protein improves murine cardiac fibrosis by preventing the accumulation of myofibroblasts. *Circ Res* 2025;**136**:26−40.
18. Li X, Pan J, Liu T, Yin W, Miao Q, Zhao Z, et al. Novel TCF21(high) pericyte subpopulation promotes colorectal cancer metastasis by remodelling perivascular matrix. *Gut* 2023;**72**:710−21.
19. Gong Z, Li Q, Shi J, Wei J, Li P, Chang CH, et al. Lung fibroblasts facilitate pre-metastatic niche formation by remodeling the local immune microenvironment. *Immunity* 2022;**55**. 1483-500.e9.
20. Hindson CM, Chevillet JR, Briggs HA, Gallichotte EN, Ruf IK, Hindson BJ, et al. Absolute quantification by droplet digital PCR *versus* analog real-time PCR. *Nat Methods* 2013;**10**:1003−5.
21. Leong DT, Gupta A, Bai HF, Wan G, Yoong LF, Too HP, et al. Absolute quantification of gene expression in biomaterials research using real-time PCR. *Biomaterials* 2007;**28**:203−10.
22. Wen Q, Huang M, Xie J, Liu R, Miao Q, Huang J, et al. lncRNA SYTL5-OT4 promotes vessel co-option by inhibiting the autophagic degradation of ASCT2. *Drug Resist Updates* 2023;**69**:100975.
23. Liu Z, Chen J, Ren Y, Liu S, Ba Y, Zuo A, et al. Multi-stage mechanisms of tumor metastasis and therapeutic strategies. *Signal Transduct Targeted Ther* 2024;**9**:270.
24. Biller LH, Schrag D. Diagnosis and treatment of metastatic colorectal cancer: a review. *JAMA* 2021;**325**:669−85.
25. Shao X, Wang Z, Wang K, Lu X, Zhang P, Guo R, et al. A single-cell landscape of human liver transplantation reveals a pathogenic immune niche associated with early allograft dysfunction. *Engineering* 2024;**36**:193−208.
26. He S, Wang LH, Liu Y, Li YQ, Chen HT, Xu JH, et al. Single-cell transcriptome profiling of an adult human cell atlas of 15 major organs. *Genome Biol* 2020;**21**:294.
27. Fleischer JR, Schmitt AM, Haas G, Xu X, Zeisberg EM, Bohnenberger H, et al. Molecular differences of angiogenic *versus* vessel co-opting colorectal cancer liver metastases at single-cell resolution. *Mol Cancer* 2023;**22**:17.
28. Gumberger P, Bjornsson B, Sandström P, Bojmar L, Zambirinis CP. The liver pre-metastatic niche in pancreatic cancer: a potential opportunity for intervention. *Cancers (Basel)* 2022;**14**:3028.
29. Houg DS, Bijlsma MF. The hepatic pre-metastatic niche in pancreatic ductal adenocarcinoma. *Mol Cancer* 2018;**17**:95.
30. Qin BF, Zhang JJ, Feng QY, Guo X, Sun HM, Song J. Specnuezhenide ameliorates hepatic fibrosis *via* regulating SIRT6-mediated inflammatory signaling cascades. *J Ethnopharmacol* 2024;**335**:118646.
31. Coll RC, Schroder K. Inflammasome components as new therapeutic targets in inflammatory disease. *Nat Rev Immunol* 2025;**25**:22−41.
32. Gaul S, Leszczynska A, Alegre F, Kaufmann B, Johnson CD, Adams LA, et al. Hepatocyte pyroptosis and release of inflammasome particles induce stellate cell activation and liver fibrosis. *J Hepatol* 2021;**74**:156−67.
33. Jia W, Liang S, Lin W, Li S, Yuan J, Jin M, et al. Hypoxia-induced exosomes facilitate lung pre-metastatic niche formation in hepatocellular carcinoma through the miR-4508-RFX1-IL17A-p38 MAPK-NF-κB pathway. *Int J Biol Sci* 2023;**19**:4744−62.
34. Yuan X, Qian N, Ling S, Li Y, Sun W, Li J, et al. Breast cancer exosomes contribute to pre-metastatic niche formation and promote bone metastasis of tumor cells. *Theranostics* 2021;**11**:1429−45.
35. Zeng Z, Li Y, Pan Y, Lan X, Song F, Sun J, et al. Cancer-derived exosomal miR-25-3p promotes pre-metastatic niche formation by inducing vascular permeability and angiogenesis. *Nat Commun* 2018;**9**:5395.
36. Qian L, Chen P, Zhang S, Wang Z, Guo Y, Koutouratsas V, et al. The uptake of extracellular vesicles: research progress in cancer drug resistance and beyond. *Drug Resist Updates* 2025;**79**:101209.
37. Lin Y, Zheng H, Jia L, Luo Y, Zhang D, An M, et al. Integrin α6-containing extracellular vesicles promote lymphatic remodelling for pre-metastatic niche formation in lymph nodes *via* interplay with CD151. *J Extracell Vesicles* 2024;**13**:e12518.
38. Nakano Y, Kamiya A, Sumiyoshi H, Tsuruya K, Kagawa T, Inagaki Y. A deactivation factor of fibrogenic hepatic stellate cells induces regression of liver fibrosis in mice. *Hepatology* 2020;**71**:1437−52.
39. Chen M, Lei X, Shi C, Huang M, Li X, Wu B, et al. Pericyte-targeting prodrug overcomes tumor resistance to vascular disrupting agents. *J Clin Investig* 2017;**127**:3689−701.
40. Fan S, Qi M, Qi Q, Miao Q, Deng L, Pan J, et al. Targeting FAPα-positive lymph node metastatic tumor cells suppresses colorectal cancer metastasis. *Acta Pharm Sin B* 2024;**14**:682−97.
41. Costa-Silva B, Aiello NM, Ocean AJ, Singh S, Zhang H, Thakur BK, et al. Pancreatic cancer exosomes initiate pre-metastatic niche formation in the liver. *Nat Cell Biol* 2015;**17**:816−26.
42. Rabas N, Ferreira RMM, Di Blasio S, Malanchi I. Cancer-induced systemic pre-conditioning of distant organs: building a niche for metastatic cells. *Nat Rev Cancer* 2024;**24**:829−49.
43. Lee W, Ko SY, Akasaka H, Weigert M, Lengyel E, Naora H. Neutrophil extracellular traps promote pre-metastatic niche formation in the omentum by expanding innate-like B cells that express IL-10. *Cancer Cell* 2025;**43**:69−85.e11.
44. Cole K, Pravoverov K, Talmadge JE. Role of myeloid-derived suppressor cells in metastasis. *Cancer Metastasis Rev* 2021;**40**:391−411.
45. Zhao S, Mi Y, Zheng B, Wei P, Gu Y, Zhang Z, et al. Highly-metastatic colorectal cancer cell released miR-181a-5p-rich extracellular vesicles promote liver metastasis by activating hepatic stellate cells and remodelling the tumour microenvironment. *J Extracell Vesicles* 2022;**11**:e12186.
46. Yang X, Zhang Y, Zhang Y, Li H, Li L, Wu Y, et al. Colorectal cancer-derived extracellular vesicles induce liver premetastatic immunosuppressive niche formation to promote tumor early liver metastasis. *Signal Transduct Targeted Ther* 2023;**8**:102.
47. Dong D, Yu X, Xu J, Yu N, Liu Z, Sun Y. Cellular and molecular mechanisms of gastrointestinal cancer liver metastases and drug resistance. *Drug Resist Updates* 2024;**77**:101125.
48. Yang W, He H, Wang T, Su N, Zhang F, Jiang K, et al. Single-cell transcriptomic analysis reveals a hepatic stellate cell-activation roadmap and myofibroblast origin during liver fibrosis in mice. *Hepatology* 2021;**74**:2774−90.
49. Puré E, Blomberg R. Pro-tumorigenic roles of fibroblast activation protein in cancer: back to the basics. *Oncogene* 2018;**37**:4343−57.
50. Qi J, Sun H, Zhang Y, Wang Z, Xun Z, Li Z, et al. Single-cell and spatial analysis reveal interaction of FAP$^+$ fibroblasts and SPP1$^+$ macrophages in colorectal cancer. *Nat Commun* 2022;**13**:1742.
51. Yang X, Lin Y, Shi Y, Li B, Liu W, Yin W, et al. FAP promotes immunosuppression by cancer-associated fibroblasts in the tumor

microenvironment *via* STAT3−CCL2 signaling. *Cancer Res* 2016;**76**: 4124−35.
52. Knorr J, Kaufmann B, Inzaugarat ME, Holtmann TM, Geisler L, Hundertmark J, et al. Interleukin-18 signaling promotes activation of hepatic stellate cells in mouse liver fibrosis. *Hepatology* 2023;**77**: 1968−82.
53. Charan HV, Dwivedi DK, Khan S, Jena G. Mechanisms of NLRP3 inflammasome-mediated hepatic stellate cell activation: therapeutic potential for liver fibrosis. *Genes Dis* 2023;**10**:480−94.
54. Wang G, Jin S, Huang W, Li Y, Wang J, Ling X, et al. LPS-induced macrophage HMGB1-loaded extracellular vesicles trigger hepatocyte pyroptosis by activating the NLRP3 inflammasome. *Cell Death Discov* 2021;**7**:337.
55. Zhou J, Song Q, Li H, Han Y, Pu Y, Li L, et al. Targeting circ-0034880-enriched tumor extracellular vesicles to impede SPP1(high)CD206$^+$ pro-tumor macrophages mediated pre-metastatic niche formation in colorectal cancer liver metastasis. *Mol Cancer* 2024;**23**:168.